



Article

In Situ Measurements of Thermal Properties of Building Fabrics Using Thermography under Non-Steady State Heat Flow Conditions

Itai Danielski * and Morgan Fröling

The Department of Ecotechnology and Sustainable Building Engineering, Mid Sweden University, SE-831 25 Östersund, Sweden; morgan.froling@miun.se

* Correspondence: itai.danielski@miun.se; Tel.: +46-(0)10-142-8716

Received: 4 May 2018; Accepted: 26 June 2018; Published: 2 July 2018



Abstract: This study describes a quantitative method using thermography to measure the thermal properties of building fabrics that are subjected to non-steady state heat flow due to consistently changing meteorological conditions. The method includes two parts. First, the convection heat transfer coefficient is measured by thermography and heat flux meters on a small segment of the examined building fabric with uniform surface temperature. Then, thermal properties of large building fabrics are evaluated by thermography. The two parts are measured simultaneously. The method was tested on 140/160/190 mm thick massive laminated spruce timber walls of a test facility cabin located in Östersund, Sweden. The results varied by only a few percent in comparison to validation measurements performed with heat flux meters and in comparison, to values from the literature. Due to rapid changes in weather conditions the measured values had large disparity, but still a linear regression with low confidence interval was obtained. Obtaining an accurate value of convection heat transfer was important for achieving high measurement accuracy and, therefore, the value of this parameter should be measured. Other important factors to consider are solar radiation, reflected infrared (IR) radiation from nearby objects and the number of thermal images.

Keywords: conductivity; building fabrics; thermal transmittance; thermal imaging; thermography; U-value; heat flux meters

1. Introduction

In an age of increasing environmental awareness and a growing demand for energy efficient buildings, the construction industry is faced with the challenge of ensuring that the energy efficiency and thermal performance projected during the design stage is achieved once a building is in use [1]. However, energy efficiency and thermal performance are rarely validated after construction or renovation. Projected values of energy indicators, such as the specific final energy demand, seldom agree with monitored final energy use after a building is constructed [1]. Danielski [2] reported a 20% difference on average between projected and measured values among newly constructed buildings in 77 locations in Stockholm. Similar results were found by Torcellini et al. [3] in six high energy-performance commercial buildings in the USA. According to Pettersen [4], it is impossible to predict the final energy demand with better accuracy than $\pm 15\text{--}20\%$, if the behaviour of a building's residents is unknown.

The discrepancy between the predicted and measured values are commonly referred to as the 'energy performance gap'. The energy performance gap can partly be explained by discrepancies between the projected and the actual values of the thermal transmittance of building fabrics (also known as the overall heat transfer coefficient or U-value). Such differences were found

by Johnston et al. [5] after in situ measurements of 25 newly constructed buildings in the UK. They anticipate that thermal performance gap is common in the existing building stock [5]. According to Menezes et al. [1] the performance gap could be reduced by knowledge acquired from post-occupancy evaluations, which could produce more accurate models of final energy demand in buildings.

Post-occupancy evaluation could include: energy monitoring, airtightness test, cavity inspection [6], co-heating tests [7], thermography and the use of measurement tools such as heat flux sensors (HFM) [8]. Airtightness tests and cavity inspections are qualitative methods used for building diagnosis. Energy monitoring can be used for evaluating energy efficiency but require up to one year to complete and may be costly. A co-heating test provides an average value of the thermal efficiency of a whole building fabric but not for a specific building element [5]. HFMs also provide a point measurement and may fail to represent the thermal performance of complete building elements.

Thermography is an additional method that is gaining popularity among the non-destructive tools for building diagnostics [9]. Since the introduction of infrared (IR) cameras in 1929, thermography has been used to address an increasing range of applications [9]. The International Energy Agency (IEA) has mentioned thermography for detecting defects in buildings in both annex 40 [10] and annex 46 [11]. The European standard EN 13187-1998 specifies a qualitative method using thermography for detecting thermal irregularities in building fabrics. Quantitative information, such as defect depths, can be retrieved as well [12]. Thermography can provide quick and accurate readings and, thus, has large potential for detection of thermal bridges [13], high moisture levels [14,15] and defects in building fabrics [16–19]. It can be used for quality control during construction of new buildings [20], development of new building insulation materials [21,22], and for investigating the condition of existing buildings, e.g., historical buildings [23,24].

Several studies have also used thermography for quantitative analysis of thermal performance of building fabrics. Ohlsson and Olofsson [25] developed a method to measure the heat flux through a wall element by a single thermal image. They achieved less than 10% uncertainty under the conditions of natural convection, but during forced convection (modelling wind) less reliable results were obtained. Their study was performed in a controlled environment with steady-state heat flow conditions.

According to Lehmann et al. [26], steady-state heat flow through building fabrics seldom occurs since buildings are exposed to consistently changing meteorological conditions [26]. Under such conditions the temperature distribution along the cross section of the wall may have a chaotic pattern with points of maximum and minimum temperature that are even warmer and colder than the surface temperature of the wall. To obtain more accurate results Albatici et al. [27] recommended use of thermography on walls facing north and east before sunrise with overcast sky. Albatici et al. [27] also recommended that the following conditions should be reached during a survey: the local wind speed near the building façade should be lower than $0.5 \text{ m}\cdot\text{s}^{-1}$, a difference of at least $15 \text{ }^{\circ}\text{C}$ between indoor and outdoor ambient air temperature should be obtained, and the outdoor temperature should have less than $6 \text{ }^{\circ}\text{C}$ temperature swing during the 12 h prior to the measurement. In similarity to steady-state heat flow, such requirements are not always possible to obtain on demand.

Fokaides and Kalogirou [28] used thermography during near steady-state conditions, in which measurement periods with relatively stable thermal conditions were selected. In their study they evaluated the thermal transmittance of different envelop elements of five buildings in Cyprus. Their results deviated by 10% to 20% in comparison with the theoretical values. Albatici et al. [27] also used thermography during near steady-state conditions to calculate the U-value of five different walls from light to heavy constructions. On average the results deviated by 26% from the modelled theoretical values and by 22% from measurements done by HFMs. Higher uncertainty in results were obtained for lightweight constructions like wooden fabrics in comparison to concrete fabrics.

Sham et al. [29] used thermography during varying weather conditions with no demand for steady-state heat flow. They monitored the exterior surface temperature of buildings in Hong Kong

and calculated the heat flow over time from building fabrics to the outdoor environment. However, no uncertainty analysis or validation of the results were reported.

From the aforementioned studies [25–29], it appears that uncertainty increases as the condition of the survey deviates from steady state. It was also apparent that the aforementioned studies are strongly relying on the temperature difference in the boundary layer between the examined object and ambient air. The conductivity of the boundary layer is described by the convection heat transfer coefficient. However, none of the aforementioned studies measured the convection heat transfer; instead they relied on values from the literature, which differs significantly among different studies [30] and were found to differ among the aforementioned studies as well. For example, for wind velocities (v) below $5 \text{ m}\cdot\text{s}^{-1}$, Ohlsson and Olofsson [25] assumed $h_{\text{Conv}} = 4\cdot v + 5.6$, Sham et al. [29] assumed $h_{\text{Conv}} = 3.9\cdot v + 5.62$, Albatici et al. [27] assumed $h_{\text{Conv}} = 3.8054\cdot v$ and Fokaides and Kalogirou [28] assumed a constant value of $h_{\text{Conv}} = 7.7 \text{ W}\cdot\text{m}^{-2}\cdot\text{K}^{-1}$. Not knowing the exact value of the convection heat transfer coefficient for each experiment conditions may impose errors in the calculations.

The aim of this study was to investigate a post-occupancy quantitative method to determine the thermal performance of building fabrics during continuously changing meteorological conditions. The method includes two stages: First, the convective heat transfer coefficient is determined using both thermography and HFMs on a small segment of the examined building fabric with uniform surface temperature. Second, based on the results from the first stage, the thermal properties of a large area of building fabric is determined by thermography. The measurements in both stages are performed simultaneously while the wall is exposed to the outdoor conditions, in which steady-state heat flow conditions are unlikely to occur.

2. Methods

The method presented in this study is based on the theory of heat transfer, which provides expressions for the calculation of conduction heat flow (Q_{Cond}), convection heat transfer (Q_{Conv}), and radiation heat flow (Q_{Rad}) under steady-state heat flow conditions. These expressions are described in Equations (1)–(3) regarding heat transfer through a wall with ϵ as the material’s emissivity and σ representing the Stefan–Boltzmann constant. h_{Cond} and h_{Conv} representing the conduction and convection heat transfer coefficients, respectively. T_{Hot} and T_{Cold} refer to different temperature measurements in each of the equations as follow: the interior and exterior wall surface temperature in Equation (1); the interior wall surface and indoor ambient air temperatures in Equation (2); and the interior wall surface and radiated temperature on the wall surface (also called the reflected temperature) in Equation (3). Equation (4) describes energy balance on a wall element during steady-state conditions.

The conduction heat transfer coefficient (h_{Cond}) is a property of bulk material, while the convection heat transfer coefficient (h_{Conv}) is a property of an interface between the wall and the ambient air. Both quantities define the thermal transmittance (U_{Small} and U_{Large}), which describes the insulation capability of a wall subjected to temperature difference between ambient air on both sides.

$$Q_{\text{Cond}} = h_{\text{Cond}}\cdot(T_{\text{Hot}} - T_{\text{Cold}}), \tag{1}$$

$$Q_{\text{Conv}} = h_{\text{conv}}\cdot(T_{\text{Hot}} - T_{\text{Cold}}), \tag{2}$$

$$Q_{\text{Rad}} = \epsilon\cdot\sigma\cdot(T_{\text{Hot}}^4 - T_{\text{Cold}}^4), \tag{3}$$

$$Q_{\text{Cond}} = Q_{\text{Conv}} + Q_{\text{Rad}}, \tag{4}$$

The method in this study takes advantage of the dynamics of real-time measurements. Transient changes of heat flux over time are not analysed, but, each measured value is considered as an independent measurement. The history prior to the measurement (e.g., changes in temperature, wind velocity, humidity, etc.) and between two subsequent thermography measurements is not considered, even if it could have a large influence on each individual measured value. Thus, each of the measured values may deviate from the expected value due to two reasons: (i) internal errors in

the measurement equipment, which cannot be avoided; and (ii) due to the non-steady state thermal conditions that are applied to steady-state equations (Equations (1)–(4)). The study analyses the overall uncertainty of the results and not the uncertainty due to each of the aforementioned errors. The hypothesis of this study is that it could still be possible to obtain accurate values of thermal properties of building fabrics using steady-state equations during non-steady state conditions by applying linear regression on a sufficiently large sample of independent measurements.

2.1. Test Object

The test object is a single-room wooden cabin with 15 m² floor area, as illustrated in Figure 1. The cabin was located about 5 m from a three-storey building to its north with no risk of shadowing from the east, south and west directions. The walls were constructed with massive glued laminated spruce timber which are kiln-dried and joined together with dowel mouldings, a technique developed by Glulam [31]. This study analyses the thermal properties of the north, east and west walls, as they were constructed with different thicknesses: 140 mm, 165 mm and 190 mm, respectively.

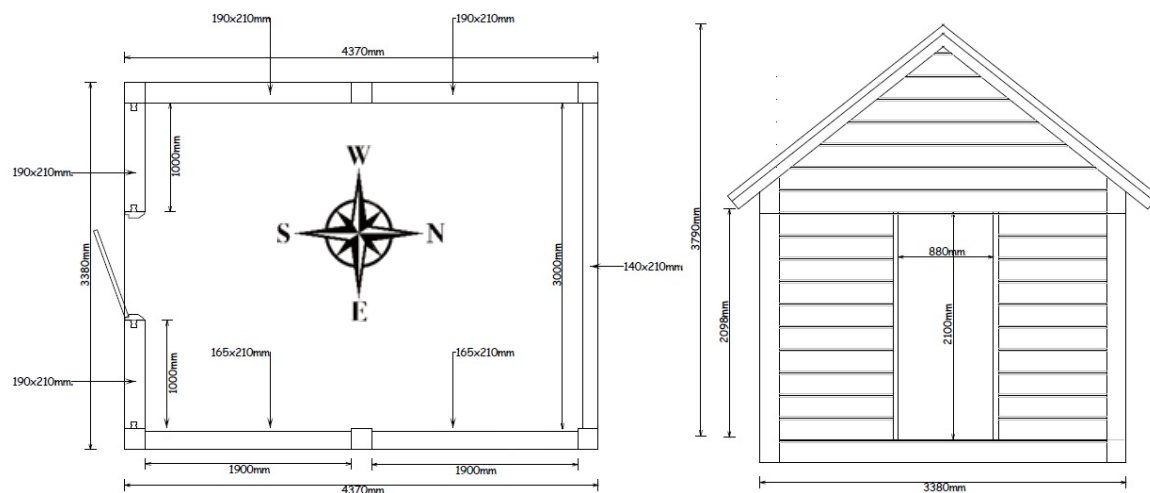


Figure 1. Schematic drawing of the wooden cabin. The test objects are the west-, north- and east-facing external walls.

During the measurement period, the cabin was heated by an electric fan heater with a max power of 2 kW connected to a thermostat, resulting in indoor temperature that fluctuated between 20 °C and 25 °C, representing living conditions. The heater was placed on the floor near the south wall; 3 m to 4 m from the measurement locations. The walls were exposed to the local outdoor weather conditions of Östersund, Sweden (63.1 °N), a subarctic climate with cold and dark winters. The temperature differences between the indoor and the outdoor environment fluctuated over the measurement period between 9 °C and 40 °C, see Appendix A. Outdoor parameters, such as wind velocity, humidity and snowfall were fluctuating as well. The temperature factor [32] at the interior surface of the walls was above 0.75 during the entire measurement period, which indicates that condensation did not occur.

2.2. Test Equipment

The measurement equipment includes: high-performance infrared camera of type FLIR T440 with resolution of 76.8 K (320 × 240 pixels), and ±2% accurate temperature measurement; and three HFMs of type HFP01 Hukseflux, 5.4 mm thick, with a nominal sensitivity of 50 μV/(W/m²), a working temperature range between −30 °C to +70 °C, and an expected typical accuracy of ±5%. The HFMs were connected to data loggers of type LI-19 from Leiderdorp Instruments. Three types of humidity and temperature loggers were used: (i) RHTemp1000 MadgeTech for outdoor ambient air measurements with working temperature between −40 °C and 80 °C, temperature resolution of 0.1 °C

and temperature calibrated accuracy of ± 0.5 °C; (ii) MicroRHTemp MadgeTech for indoor ambient air measurements with working temperature between 0 °C and 60 °C, temperature resolution of 0.1 °C and temperature calibrated accuracy of ± 0.5 °C; and (iii) ELOG9004 for wall surface measurements with temperature resolution of 0.5 °C and temperature calibrated accuracy of ± 0.5 °C.

2.3. Experiment Settings

Figure 2 illustrates the experiment configuration. Thermal images were taken at the interior surface of each wall at a distance of at least 0.5 m from the corners to include only laminar heat flow through the walls. The IR camera was located two meters from the wall at an angle of 15° to avoid its own reflection on the wall. Each thermal image was measured simultaneously: the surface temperature of a small wall segment of 0.1 m \times 0.1 m ($T_{\text{Small_wall}}$), the surface temperature of a large wall segment of 1 m \times 0.6 m ($T_{\text{Large_wall}}$), and the reflected temperature ($T_{\text{Reflected}}$). $T_{\text{Reflected}}$ was measured with a crinkled aluminium foil near the measurement area, as described in [33]. The thermal images were analysed by the FLIR-Tools software from FLIR System Inc.

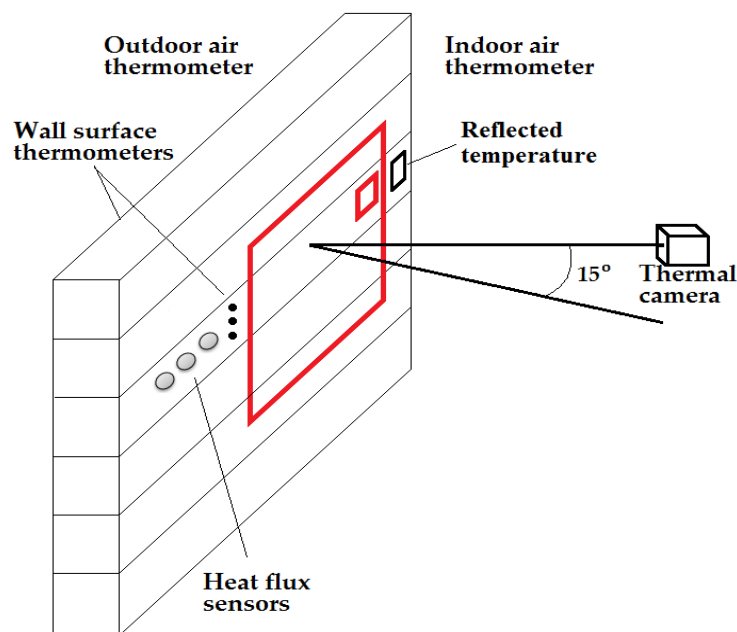


Figure 2. Experiment settings on a massive wood wall element including the locations of the sensors and the thermal camera. Each thermal image includes measurements of the reflection temperature (small black square) and the surface temperature of the large wall segment (large red square) and the small wall segment (small red square).

Three HFMs were used to obtain three independent measurements. The HFMs were calibrated by the manufacturer before the measurements. To obtain continuous contact to the walls without air cavities, the HFMs were lubricated with a thin layer of Dow 340 heat sink compound. The Dow 340 heat sink compound have low thermal resistance and are assumed to have a minor effect on the thermal properties of the wall. The HFMs were located on a wall surface with uniform temperature. The location was chosen by scanning the walls with IR camera before the installation. The emissivity of the HFMs (0.95) is similar to the emissivity of the walls.

Three ELOG9004 were installed on the inner side of the wall and two on the outer side to measure the wall's interior and exterior surface temperature. RHTemp1000 registered the outdoor temperature (T_{Outdoor}) and five MicroRHTemp registered the indoor temperatures (T_{Indoor}). The measurement locations of the reflected temperature, HFM sensors and temperature sensors were near the location of

the thermal images at the same height as the small wall segment, as illustrated in Figure 2, and did not affect the thermography measurements.

2.4. Measurements

Two to three thermal images were taken per day for each wall at arbitrary hours during a period of two months. The temperature time lag of the wooden cabin is estimate to be between 4–6 h (see Appendix B), which is shorter than the daily measurement period. The reason for the low rate of measurements was to obtain a change in meteorological conditions between successive images. Heat flux through the wall and wall surface temperature were measured in three periods, one measurement period for each wall, as listed in Table 1.

Table 1. Measurement periods of the small and large wall segments, as illustrated in Figure 2.

Measured Wall	Convection Heat Transfer Coefficient (h_{Conv}) Measured on a Small Wall Segment Using Thermography and Heat Flux Sensors (HFMs)	Thermal Properties (U_{Large} and C) Measured on a Large Wall Segment, Using Thermography
North	Period I: 24 January–15 February	24 January–22 March
East	Period II: 17 February–8 March	24 January–22 March
West	Period III: 9 March–22 March *	24 January–22 March ¹
North wall: near steady-state	Period IV: 5 May–11 June	-----

¹ Thermal images taken between 9 and 22 March for the large wall segment were not considered as many of them were found to be affected by direct solar radiation, see Section 3.2. Only a small part of the values of the HFM measurements were affected by direct solar radiation.

A fourth measurement period using HFMs and temperature sensors was used for validation purposes with near steady-state heat flow conditions, as will be described in Section 2.5. The meters were configured to collect measurements with 15 min intervals. The following thermal properties were determined for each wall using Equations (5)–(7) that were developed from Equations (1)–(4):

First, the convection heat transfer coefficient (h_{Conv}) was determined separately for each wall using both thermography and HFMs during the corresponding measurement period, as listed in Table 1. The convection heat transfer coefficient (h_{Conv}) was determined by a linear regression of the convection heat flow (Q_{Conv}) against the difference between the indoor temperature and the interior surface temperature of the small wall segment area $\Delta(T_{Indoor} - T_{Small_wall})$. The convection heat flow (Q_{Conv}) was calculated according to Equation (5). The conduction heat flow through the wall (Q_{Cond}) was measured simultaneously by three HFMs. The interior surface temperature on the small wall segment (T_{Small_wall}) was measured by thermography. The emissivity (ϵ) of the wood was 0.91; it was measured using the thermography of similar wood material covered partly by black tape with known emissivity (0.95) as describe in [34].

$$Q_{Conv} = Q_{Cond} - \epsilon \cdot \sigma \cdot (T_{Reflection}^4 - T_{Small_wall}^4), \tag{5}$$

After obtaining the value of the convection heat transfer coefficient (h_{Conv}), as described above, the thermal transmittance of the small wall segment (U_{Small}) could be determined by a linear regression of the conduction heat flow through the small wall segment ($Q_{Cond,Small_wall}$) against the difference between the indoor and outdoor temperatures $\Delta(T_{Indoor} - T_{Outdoor})$. $Q_{Cond,Small_wall}$ was calculated according to Equation (6) using the IR camera and indoor temperature sensors. Equations (5) and (6) are used to compare consistency between the results of the HFM and thermography on the small wall segment, separately for each wall. The thermography and the HFMs were both applied on a similar size of wall area and with similar uniformity of wall surface temperature.

The results from thermography of the north wall were also compared to later measurements using HFMs during near steady-state conditions, as will be described in Section 2.5.

$$Q_{Cond,Small_wall} = h_{conv} \cdot (T_{Indoor} - T_{Small_wall}) + \epsilon \cdot \sigma \cdot (T_{Reflected}^4 - T_{Small_wall}^4), \tag{6}$$

Then, the thermal transmittance of the large wall segment (U_{Large}) was determined by a linear regression of the conduction heat flow through the large wall segment ($Q_{\text{Cond, Large_wall}}$) against the difference between the indoor and outdoor temperatures $\Delta(T_{\text{Indoor}} - T_{\text{Outdoor}})$. $Q_{\text{Cond, Large_wall}}$ was calculated according to Equation (7) using the IR camera and indoor temperature sensors. The results were compared to the thermal transmittance measured for the small wall segment to evaluate the thermal effects of thermal inhomogeneities in the walls.

$$Q_{\text{Cond, Large wall}} = h_{\text{conv}} \cdot (T_{\text{Indoor}} - T_{\text{Large_wall}}) + \epsilon \cdot \sigma \cdot (T_{\text{Reflected}}^4 - T_{\text{Large_wall}}^4), \quad (7)$$

The thermal conductance (C) and the conductivity (λ) of the wood beams were also determined by thermography for each wall by a linear regression of the conduction heat flow through the small wall segment ($Q_{\text{Cond, Small_wall}}$) (Equation (6)) against the difference between the interior and exterior wall surface temperatures. The conductivity (λ) was calculated by Equation (8) with L as the wall thickness. The conductivity of the different walls was compared as they are all made by the same wood material, and thus expected to have similar values.

$$\lambda = C \cdot L, \quad (8)$$

2.5. Near Steady-State Conditions

The HFMs and the temperature sensors were used during a fourth measurement period (as listed in Table 1) in which near steady-state conditions were reached. The north wall was measured since it was the less effected by solar radiation. One HFM was installed on each side of the wall and registered the heat flux with 15 min interval. The set point of the indoor thermostat was increased to 30 °C to allow a sufficient difference between the indoor and outdoor temperatures.

Of all the measurement values, only measurement periods with near steady state were selected. Near steady state was considered if all the three following conditions were fulfilled: (i) the difference between heat flux measured at the interior and exterior wall surface was less than 10%; (ii) the change in indoor temperature during three hours prior to the measurement reading was less than 1 °C; and (iii) the change in outdoor temperature during three hours prior to the measurement was less than 1 °C. The fourth measurement period included a total of 3514 measurement readings with 15 min interval; of these, only 260 measurement readings (7%) fulfilled the requirements of near steady-state conditions.

2.6. Number of Measurements

To evaluate the minimum number of thermal images that are needed to obtain adequate results, the uncertainty in the value of the thermal transmittance was analysed with regards to the number of measurements in the linear regression. The thermal transmittance of the large wall segment (U_{Large}) of the north wall was determined with a different number of thermal images ranging from 1 to 80 and with different combinations out of a total of 115 thermal images. The dispersion of the results and the uncertainty in relation to the expectation value of thermal transmittance were calculated for each set of thermal images.

3. Results

3.1. Thermal Images

A total of 134 thermal images were taken for each wall during the first three measurement periods. Figure 3 illustrates a representative example of thermal images of the three walls. The measurement areas of both the small wall segment and the large wall segment are marked with a large and a small rectangle, respectively. Table 2 lists the minimum, maximum, average temperatures and temperature uniformity for all three images. Temperature uniformity was calculated considering the temperature reading of each pixel in the thermal image.

The temperature uniformity of the small area segments was 99.7% in all three images in Figure 3. Lower uniformity was found for the large wall segments in all three images due to thermal inhomogeneities like wood knots (illustrated by the dark spots in Figure 3) and contact areas between the wood beams (illustrated by the dark horizontal lines in Figure 3). These patterns were found in all thermal images. Higher temperature on the interior wall surface were measured for walls with larger thickness, as expected. The east wall was found to have the lowest temperature uniformity. The reason is the darker area in the left side of the image, caused by reflection from the colder north wall. Similar temperature patterns were found in most of the images of the east wall due to the position of the infrared camera. A vertical temperature gradient is also apparent in each of the three images illustrated by darker colures in the bottom of each image due to the vertical gradient in indoor ambient air temperature.

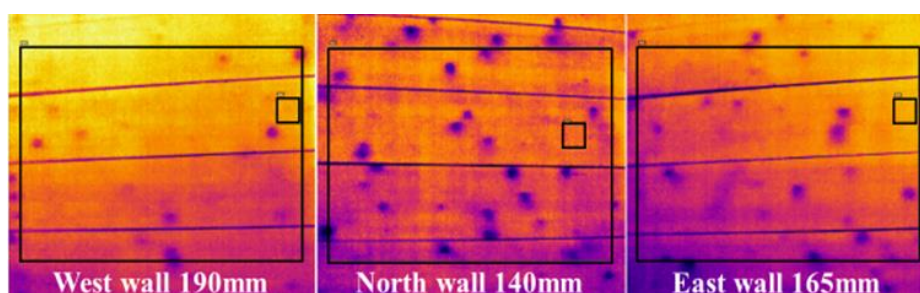


Figure 3. Representative example of thermal images of the three walls taken 1st of February. The indoor and outdoor temperatures at the time were 21.2 °C and −7.5 °C, respectively. The temperature scale in each image ranges from 15 °C to 19 °C. The darker areas represent colder surface temperatures.

Table 2. Temperature statistics obtained from the thermal images in Figure 3.

	West Wall		North Wall		East Wall	
	Small Segment	Large Segment	Small Segment	Large Segment	Small Segment	Large Segment
Min.	17.9 °C	16.2 °C	17.2 °C	15.0 °C	17.7 °C	15.7 °C
Max.	18.4 °C	18.8 °C	17.5 °C	17.8 °C	18.1 °C	18.2 °C
Average	18.2 °C	18.1 °C	17.4 °C	17.3 °C	17.9 °C	17.5 °C
Standard deviation	0.055	0.29	0.052	0.225	0.054	0.298
Uniformity ¹	99.7%	98.4%	99.7%	98.7%	99.7%	98.3%

¹ The uniformity values are based on temperatures in Celsius and are suited for relative comparisons only. Uniformity = 1 – Standard deviation/Average.

The value of the reflected temperature, measured on the three walls by thermography (not shown in Figure 3), followed roughly the changes in indoor temperature. The time lag could not be determined as it was shorter than the time between two subsequent thermal images (2–3 h), which signify the difficulty in reaching steady-state heat flow due to the high thermal inertia of the inner wall surfaces and, probably, of the outer wall surfaces as well.

3.2. Convection Heat-Transfer Coefficient

The thermal transmittance is based on Equations (6) and (7) for the small and large wall segments, respectively. These equations rely on two modes of heat transfer to the walls, i.e., by radiation and convection. The amount of heat transfer by the convection mode was found to be more significant in comparison to heat transfer by the radiation mode for all three walls. Assuming different values of the convection heat transfer coefficient in Equations (6) and (7) significantly affected the results of the different thermal properties of the walls, which stress the importance of determining the value of the convection heat-transfer coefficient by measurements.

During the measurement period, the wooden cabin was empty, and any changes over time in the value of the convection heat-transfer coefficient, on the interior surface of the walls, is due to changes in the temperature difference between the wall surface and the indoor ambient air, which were 5 °C at its highest in all three measurement periods (Table 1). Therefore, the values of the convection heat transfer are averages over each measurement period (2–3 weeks), but due to the small temperature difference it is possible to assume that the values are representative. The convection heat transfer at the small and large wall segments was assumed to be similar, since the surfaces and geometry are similar.

The convection heat-transfer coefficients (h_{Conv}) of the three walls were determined through regression analysis, as illustrated in Figure 4, with forced intercept $(X, Y) = (0, 0)$. The values obtained for the north and east walls differed by less than 1%. The convection heat-transfer coefficient of the west wall was 11% higher in comparison to the values of the north and east walls. The reason was the effect of direct solar radiation on the temperature of the interior and exterior surfaces of the west wall during the third measurement period (Table 1). Hereafter the value of the convection heat-transfer coefficient of the west wall was assumed to be the average of the convection heat-transfer coefficients of the north and east walls since all three walls were subjected to similar indoor and outdoor conditions.

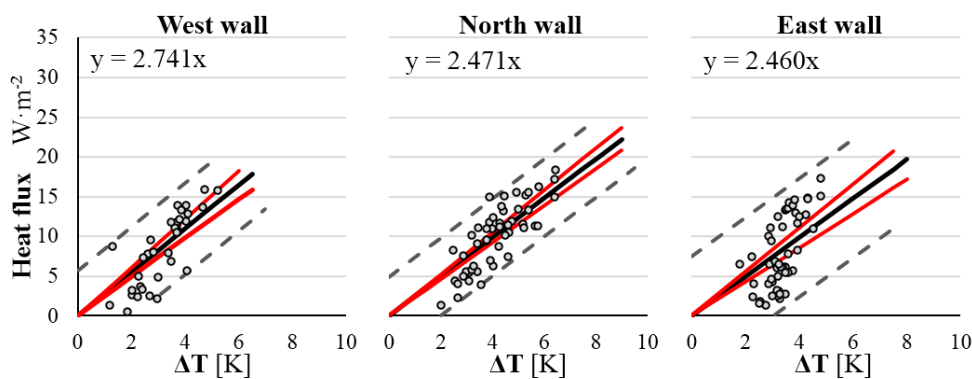


Figure 4. The convection heat transfer coefficient of the west wall (left figure), north wall (middle figure) and east wall (right figure) with confidence interval of 95% certainty (red lines). The Y-axis represents the convection heat transfer (Q_{Conv}) calculated by Equation (5). The X-axis represent the temperature difference between the indoor temperature and the interior wall surface $\Delta T = (T_{Indoor} - T_{Small_wall})$. The dashed lines represent 95% certainty for measurements to disperse around the mean (black trend-line).

3.3. Thermal Transmittance: Small Wall Segment

Figure 5 illustrates a regression analysis to determine the thermal transmittance of the small wall segment for the north wall undertaken with HFMs and thermography. The values of thermal transmittance obtained by thermography differed by 1% in comparison to the values obtained by HFMs for all walls. The thermal transmittance of the north wall obtained by HFMs during near steady-state heat flow was higher by 2% in comparison to the value obtained by thermography, as illustrated in Figure 5 and also in Figure 8.

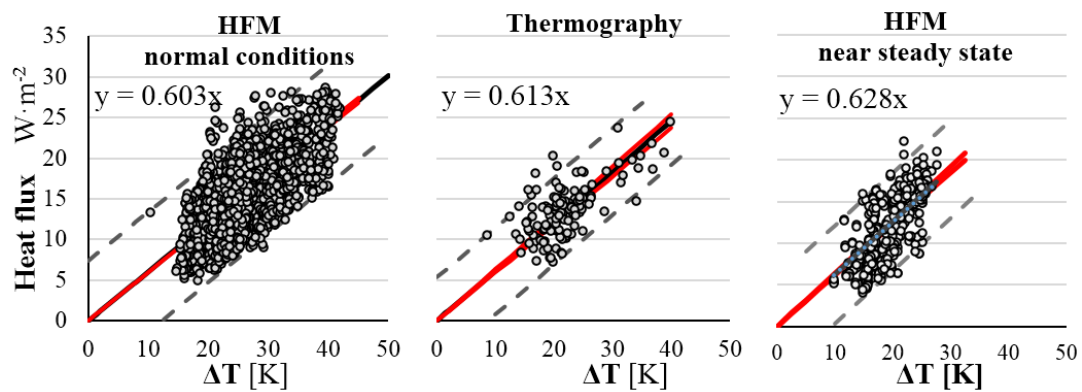


Figure 5. The thermal transmittance of the small wall segment for the north wall determined using heat flux sensors (HFMs) (left figure), thermography (centre figure) and HFMs during near steady-state conditions (right figure) with confidence interval of 95% certainty (red lines). The Y-axis represents the conduction heat flux Q_{Cond} measured by HFMs (right and left figures) or $Q_{Cond,Small}$ wall calculated by Equation (6) for thermography (centre figure). The X-axis represents the difference between the indoor and outdoor ambient air temperatures, $\Delta T = (T_{Indoor} - T_{Outdoor})$. The dashed lines represent 95% certainty for measurements to disperse around the mean (black trend-line).

3.4. Thermal Transmittance: Large Wall Segment

Figure 6 illustrates a regression analysis to determine the thermal transmittance of the large wall segment (U_{Large}) for all three walls using thermography. The thermal transmittance of the north and west walls were 3% and 5% higher in comparison with the respective thermal transmittance of the small wall segment. The reason is most likely to be thermal inhomogeneities like wood knots and contact areas between the wood beams, as illustrated in Figure 3. The thermal transmittance of the east wall was 20% higher in comparison with the thermal transmittance of the small wall segment. Thermal inhomogeneities may have a similar effect here as well, but the larger part of the difference is most likely a measurement error in the value of the reflection temperature, which was not uniform over the east wall as is seen in Figure 3, and thus was difficult to evaluate.

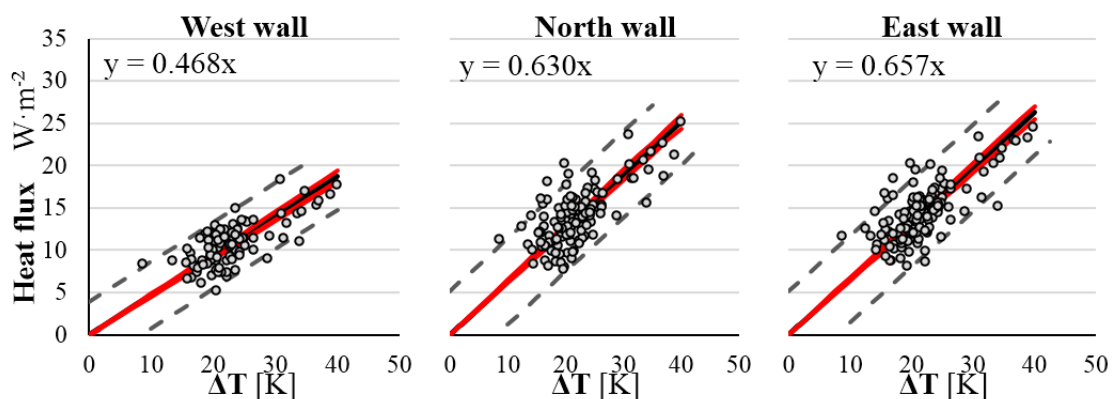


Figure 6. The thermal transmittance of the large wall segment calculated using thermography for the west wall (left figure), north wall (centre figure) and east wall (right figure) with confidence interval of 95% certainty (red lines). The Y-axis represents the conduction heat transfer ($Q_{Cond, Large_wall}$) calculated by Equation (7). The X-axis represents the difference between the indoor and outdoor ambient air temperatures, $\Delta T = (T_{Indoor} - T_{Outdoor})$. The dashed lines represent 95% certainty for measurements to disperse around the mean (black trend-line).

3.5. Thermal Conductance and Conductivity

Figure 7 illustrates the thermal conductance of the small wall segment for each of the three walls. As expected, the thermal conductance decreases with thicker walls. The conductivity of the west, north and east walls were $0.101 \text{ W}\cdot\text{m}^{-1}\cdot\text{K}^{-1}$, $0.105 \text{ W}\cdot\text{m}^{-1}\cdot\text{K}^{-1}$ and $0.108 \text{ W}\cdot\text{m}^{-1}\cdot\text{K}^{-1}$, respectively, as illustrated in Figure 8.

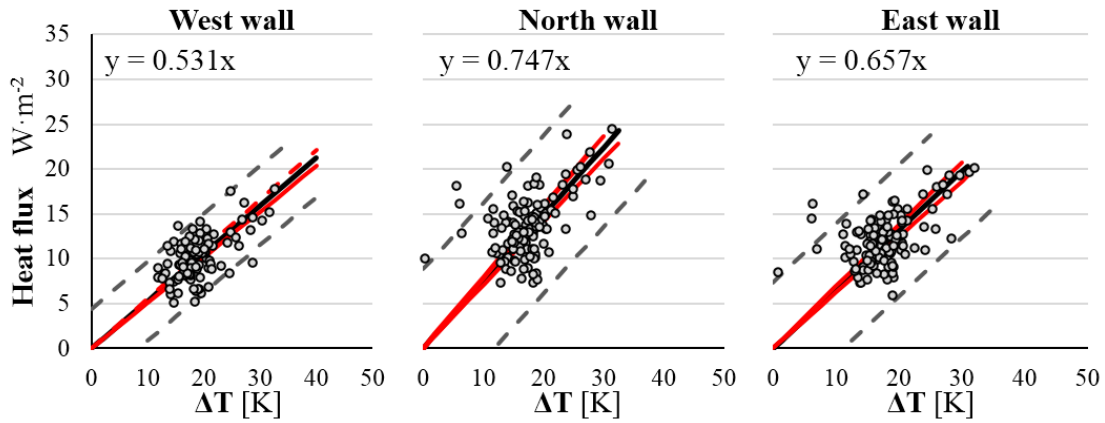


Figure 7. The thermal conductance of the west wall (left figure), north wall (centre figure), and east wall (right figure) with confidence interval of 95% certainty (red lines). The Y-axis represents the conduction heat transfer ($Q_{\text{Cond,Small_wall}}$) calculated by Equation (6). The X-axis represents the difference between the interior and exterior wall surface temperatures. The dashed lines represent 95% certainty for measurements to disperse around the mean (black trend-line).

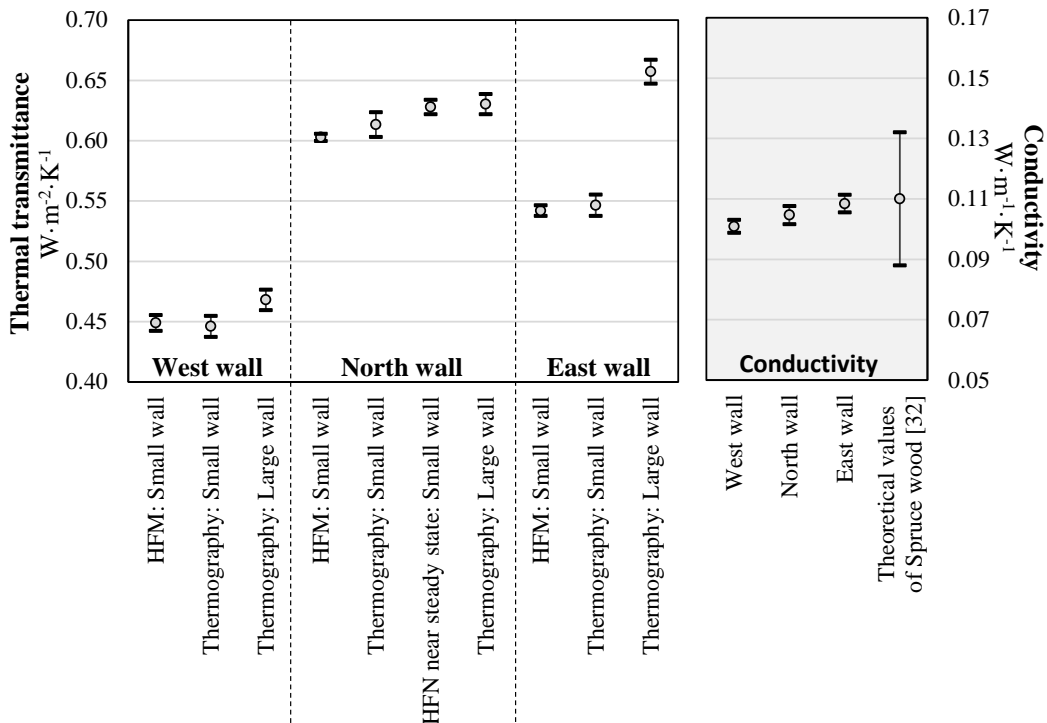


Figure 8. Summary of the main results: the thermal transmittance and the conductivity of the west, north and east walls. Uncertainties of the measurements are represented by the error bars.

3.6. Number of Measurements

Figure 9 illustrates the effect of number of measurements (thermal images) on the value of the thermal transmittance and uncertainty of the north wall. The uncertainty decreases and the value of the thermal transmittance is converging with larger number of thermal images taken. A single thermal image was found to have more than 100% uncertainty. The skewed distribution with low number of thermal images is caused by one high measurement value (see also Appendix C). Already after 10 thermal images the distribution is symmetrical around its mean value with uncertainty of 10%. A regression analysis using 27 and 63 thermal images reduced the uncertainty to 5% and 3%, respectively.

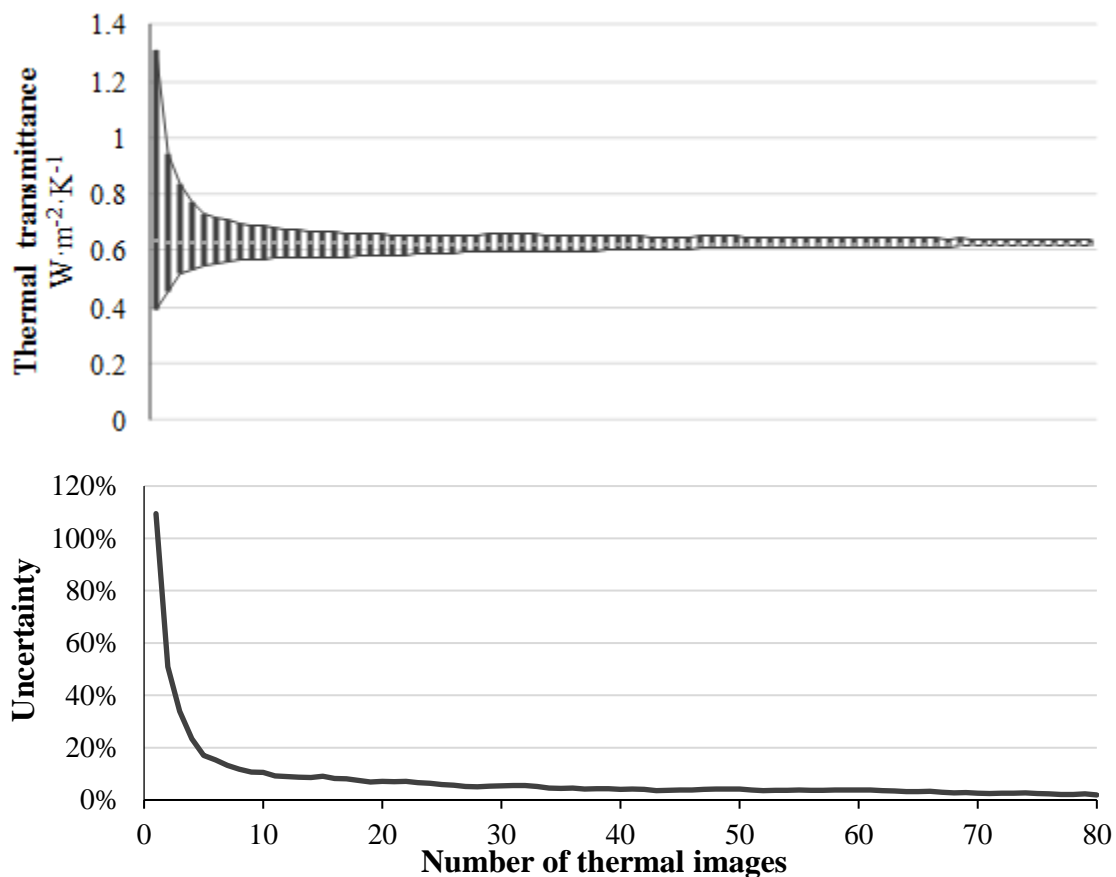


Figure 9. The span of values of thermal transmittance (upper figure) and the uncertainty in values of thermal transmittance (lower figure) vs. the number of measurements (thermal images).

4. Discussion

In this study, thermography was used to measure the thermal properties of massive wooden walls of glued laminated spruce timber with different thicknesses that were exposed to varying outdoor weather conditions. Thus, the walls were subjected to non-steady state heat flow conditions during the measurement periods. The non-steady state heat flow and the errors of the measurement equipment resulted in large dispersion of individual measurement results. Still, linear regressions on all measurement values gave a low confidence interval around the mean values.

Measurements undertaken using thermography were less dispersed but with a slightly higher confidence interval around the mean in comparison to measured values by HFMs. This is because the confidence interval is significantly affected by the measurement sample size. Determining the thermal transmittance with a single thermal image has more than 100% uncertainty. Less than 10%

uncertainty could be achieved by 10 or more thermal images. To achieve less than 5% uncertainty, at least 27 thermal images are needed.

Today's IR cameras can be programmed to capture thermal images automatically with time intervals of a few seconds to one image per day. In this study, the sampling rate of thermal images was intentionally low to obtain changes in meteorological conditions between successive images. In practice, a higher sampling rate could be applied, which would significantly shorten the measurement period. There are also IR cameras with better resolution on the market, which may provide more accurate results, or alternatively can be used to evaluate larger building elements.

The convection heat transfer coefficient was another key factor for obtaining accurate results. It was calculated by using both HFMs and thermography on a small wall segment and was $2.47 \text{ W}\cdot\text{m}^{-2}\cdot\text{K}^{-1}$ for the north wall and $2.46 \text{ W}\cdot\text{m}^{-2}\cdot\text{K}^{-1}$ for the east wall with $\pm 3\%$ and $\pm 6\%$ uncertainty, respectively. Due to the effect of solar radiation, the value of the convection heat transfer coefficient of the west wall was 12% to 14% higher. The reason was the effect of direct solar radiation on the temperature of the interior surface of the west wall during the third measurement period. These values seem to be in the lower range of values in comparison to values assumed in similar studies [25,27–29]. However, values of convection heat transfer coefficients depend strongly on the experiment's specific conditions and settings. These can vary considerably among studies [30], e.g., wind velocity, surface texture, tilt of surfaces, temperature, and near objects. Therefore, comparisons to literature values should be made with caution.

The values of thermal transmittance obtained by thermography and HFMs on a small wall segment with uniform temperature differed by less than 1%, which suggest that the two measurement methods are compatible on surfaces with high temperature uniformity. However, values of thermal transmittance measured on a large wall segment using thermography were 3% to 5% higher in comparison to the thermal transmittance measured on a small wall segment. The reasons were thermal inhomogeneities like wood checks and knots and the contact areas between the wood beams.

The results demonstrate the main advantage of thermography over spot measurements, for example by HFMs. The results of spot measurements are strongly affected by the position of the measurement and, therefore, not representative. Thermography enables measurement of average values of large areas of building fabrics, accounting for all thermal inhomogeneities. Thermal inhomogeneities in large building elements and could also include different structures or materials with different thermal properties. The suggested method could account for these thermal inhomogeneities, and still provide representative average values of thermal transmittance for the entire building element.

Values of thermal transmittance measured by HFMs during near steady-state heat flow conditions were 2% higher in comparison to values obtained by thermography. Near steady-state measurements were performed during a period with warmer weather conditions; 7 °C higher in average both indoor and outdoor. According to Glass and Zelinka [35], the conductivity of wood increases by about 2% to 3% with a temperature increase of 10 °C due to the absorption of moisture in the wood, which could be the reason for the 2% difference in values.

The conductivity of wood can also vary with temperature and humidity levels, which affect the water content in the wood. Thus, literature values of wood conductivity should be used with caution as actual conductivity values may vary by as much as 20% [35]. Still, a good agreement was attained between the experimental result and the reference literature values [35], as illustrated in Figure 8, even if the obtained measurement values had large dispersion due to the varying thermal conditions, as illustrated in Figures 5 and 6.

The conductivities of the small wall segments of the west, north and east walls deviated by 9%, 5% and 2%, respectively in comparison to the conductivity of spruce wood from the literature ($0.11 \text{ W}\cdot\text{m}^{-1}\cdot\text{K}^{-1}$) [35]. The conductivities of the large wall segments could not be determined since the temperature of the exterior surface of the large wall segment were not measured. But the values are expected to be higher by 3% to 5% in comparison to the conductivity of the small wall segment

due to the inhomogeneities, as was shown in Section 3.1. Thus, the conductivity values of the large wall segment are expected to be $0.106 \text{ W}\cdot\text{m}^{-2}\cdot\text{K}^{-1}$, $0.108 \text{ W}\cdot\text{m}^{-2}\cdot\text{K}^{-1}$ and $0.113 \text{ W}\cdot\text{m}^{-2}\cdot\text{K}^{-1}$ for the west, north and east walls with 6%, 2% and 3% deviation from the literature value [35], respectively.

To obtain representative temperature readings by IR camera, thermal images of wall surfaces need to be corrected for the reflected radiation. The reflected radiation holds information about the temperature of nearby objects but not of the wall itself. The reflected radiation should be uniform on the measured surface area, otherwise it could not be determined. In this study, the gradient in reflected temperature on the interior surface of the east wall was found to impose a large error in the measurements. The temperature gradient due to reflected radiance from surrounding objects could be avoided by a better camera position.

The method described in this study was applied to 140 mm, 165 mm and 190 mm thick massive wooden walls. Thermal images were taken in a rate of two to three images per day. Further studies are needed to evaluate the applicability of the method on other types of wall fabrics, to determine the limits of the method in terms of minimum ambient temperature difference between the indoor and outdoor and the minimum heat flow through the building element, and to evaluate the minimum rate of measurement sampling in order to reduce the total measurement time. Additional studies are also needed regarding the effects of solar radiation and night sky thermal exchange.

5. Conclusions

Thermography is a non-destructive method that can evaluate thermal properties of large building fabrics, accounting for all thermal inhomogeneities. In this study a method using thermography was tested to measure thermal properties of building fabrics that are exposed to a varying outdoor condition, i.e., no need to attain steady-state heat flow. The method includes two stages: first, the convective heat transfer coefficient is determined using both thermography and heat flux meters; then, the thermal properties of large building fabric are determined solely by thermography. The two stages are performed simultaneously.

During the testing of the method a few key issues were identified: the value of the convective heat-transfer coefficient was found to have large effect on the results and, therefore, should be measured. The position of the infrared camera is important and should be adjusted to obtain uniform reflected temperature from the surrounded objects. Sufficient numbers of measurement are needed to obtain accurate results, and direct solar radiation on the measured building fabric should be avoided.

This study demonstrated the main advantage of thermography over spot measurements. Thermography enables measurement of average thermal properties of large areas of building fabrics, accounting for all thermal inhomogeneities, like different structures and materials, while spot measurements are strongly affected by the position of the measurement.

The results of this study indicate that thermography has a potential to be used as a tool for post-occupancy evaluation of thermal properties of building fabrics with high precision. The method used in this study was tested with the following conditions. The building elements were massive wood walls with different thicknesses. The ΔT between the indoor and outdoor temperatures varied from $10 \text{ }^\circ\text{C}$ to $40 \text{ }^\circ\text{C}$, see Appendix A. The global solar irradiation varied during the three measurement periods from as low as $50 \text{ W}/\text{m}^2$ up to $400 \text{ W}/\text{m}^2$, see Appendix A.

The experiment in this study was design to examine if it is possible to measure thermal properties of building elements during conditions of non-steady state heat flow with an IR camera. Therefore, a simple setup of one wall material was used, and the limitations of the method still need to be determined. These could include other types of wall fabrics and thermal properties, testing for periods with lower ΔT , lower rate of measurement sampling, and correction for the effect of higher global solar irradiation.

Author Contributions: Conceptualization, I.D.; Data curation, I.D.; Formal analysis, I.D.; Investigation, I.D.; Methodology, I.D.; Resources, I.D.; Supervision, M.F.; Validation, I.D.; Visualization, I.D. and M.F.; Writing—original draft, I.D. and M.F.; Writing—review and editing, I.D. and M.F.

Funding: This research received no external funding.

Acknowledgments: The authors would like to thank Glulam of Sweden AB and MRD Säljö Bygg AB for their contribution for this study in materials and equipment. Special thanks for Anders Lundström and Åke Mård for their time and engagement.

Conflicts of Interest: The authors declare no conflict of interest. The founding sponsors had no role in the design of the study; in the collection, analyses, or interpretation of data; in the writing of the manuscript, and in the decision to publish the results.

Nomenclature

Q_{Cond}	Conduction heat flow, $\text{W}\cdot\text{m}^{-2}$
Q_{Conv}	Convection heat flow, $\text{W}\cdot\text{m}^{-2}$
Q_{Rad}	Radiation heat flow, $\text{W}\cdot\text{m}^{-2}$
$Q_{\text{Cond,Small_wall}}$	Conduction heat flow through a small wall segment, $\text{W}\cdot\text{m}^{-2}$
$Q_{\text{Cond,Large_wall}}$	Conduction heat flow through a large wall segment, $\text{W}\cdot\text{m}^{-2}$
h_{Cond}	Conduction heat transfer coefficient, $\text{W}\cdot\text{m}^{-2}\cdot\text{K}^{-1}$
h_{Conv}	Convection heat transfer coefficient, $\text{W}\cdot\text{m}^{-2}\cdot\text{K}^{-1}$
T_{Outdoor}	Ambient outdoor temperature, K
T_{Indoor}	Ambient indoor temperatures, K
$T_{\text{Small_wall}}$	Surface temperature of a small wall segment, K
$T_{\text{Large_wall}}$	Surface temperature of a large wall segment, K
$T_{\text{Reflected}}$	Reflected temperature, K
T_{Ext}	Surface temperature on the exterior side of the wall
ϵ	Emissivity
σ	Stefan–Boltzmann constant
U_{Small}	Thermal transmittance of the small wall segment, $\text{W}\cdot\text{m}^{-2}\cdot\text{K}^{-1}$
U_{Large}	Thermal transmittance of the large wall segment, $\text{W}\cdot\text{m}^{-2}\cdot\text{K}^{-1}$
C	Thermal conductance, $\text{W}\cdot\text{m}^{-2}\cdot\text{K}^{-1}$
λ	Conductivity, $\text{W}\cdot\text{m}^{-1}\cdot\text{K}^{-1}$

Appendix A. Indoor and Outdoor Temperatures

Figure A1 represents the indoor and outdoor temperatures during the three measurement periods. For experimental set up, see Section 2. Methods in the main article. During the 1st measurement period (24 January–15 February), the outdoor temperature had the lowest values and the largest variations. This period is also characterised by low global solar irradiation (about $50 \text{ W}/\text{m}^2$) and short daytime (6 to 8 h per day). The effect of the solar irradiation is minor, and therefore no cyclic variations in outdoor temperature were observed between day and night during this period.

During the 2nd measurement period, solar irradiation is a bit stronger and cyclic variations in outdoor temperature are observed sporadic, depending on cloud formation. During the 3rd measurement period, cyclic variations of outdoor temperature between day and night are clearly observed. This is due to the effect of the solar irradiation, with global solar irradiation of about $400 \text{ W}/\text{m}^2$ and daytime of about 12 h.

The indoor temperature also alternates between $20 \text{ }^\circ\text{C}$ and $25 \text{ }^\circ\text{C}$ during the three measurement periods (Figure A1). As a result, the value of the temperature difference between the indoor and outdoor (Figure A2) was constantly changing during the entire measurement period, which reduces the chances for steady-state heat flow conditions.

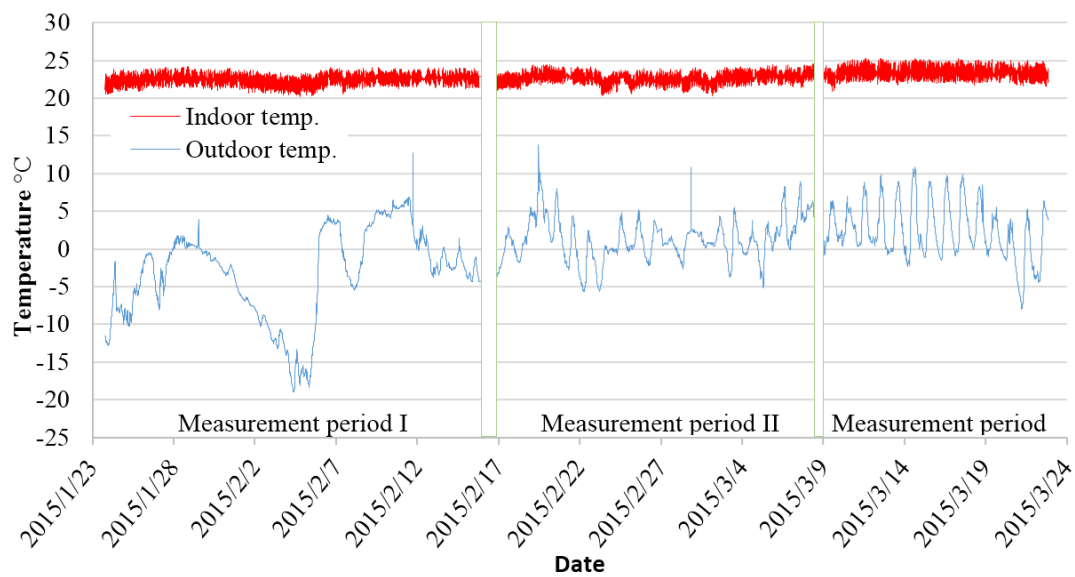


Figure A1. The indoor and outdoor ambient air temperatures with 15 min sampling interval between measurements.

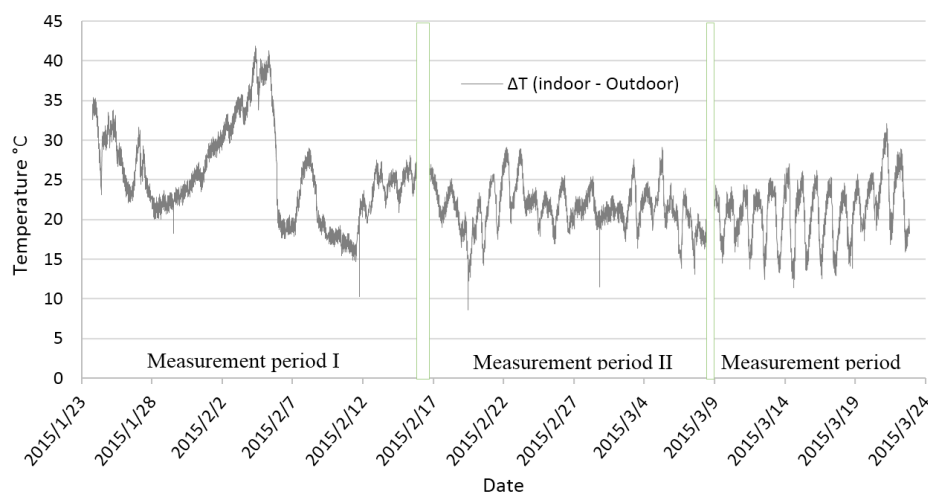


Figure A2. The difference between the indoor and outdoor ambient air temperature with 15 min sampling interval between measurements.

Appendix B. Reflected and Indoor Temperatures

Figure A3 illustrates the indoor temperature and the reflected temperature measured on the three walls during the three measurement periods. For experimental set up, see Section 2. Methods in the main article. During the entire measurement period, the reflected temperatures of the three walls were lower than the indoor temperature by a few degrees centigrade. Both the indoor temperature and the reflected temperature of the three walls have similar increases in values with time (see trend-lines in Figure A3). The reflected temperature of the North wall was found to be slightly lower in average in comparison to the reflected temperature of the East and West walls. The reason could be exchange of radiation with the parallel south wall, with its built-in entrance door, as illustrated in Figure 1 in the main article. From a comparison between the indoor temperature in Figure A3 and the outdoor temperature in Figure A1, it is possible to estimate that the temperature time lag of the wooden cabin is in the range of 4–6 h.

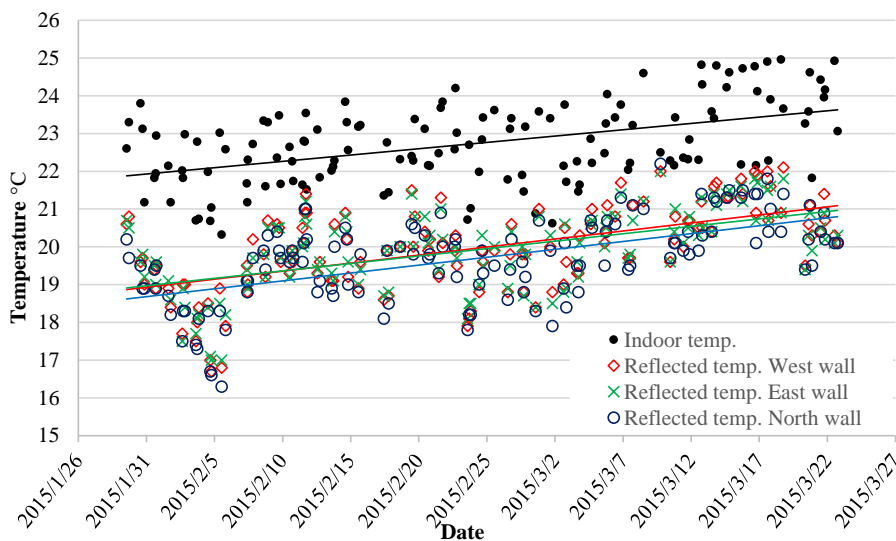


Figure A3. The indoor temperature and the reflected temperature measured on the three walls during the three measurement periods with 15 min sampling interval between measurements.

Appendix C. Number of Measurements

Figure 9 in the main article illustrates the range of values of thermal transmittance and the uncertainty with regards to the number of thermal images used in the linear regression. Figure A4 in this appendix section illustrates the distribution of the values of the thermal transmittance in form of histograms plots. Each plot represents the results from a regression analysis with a different number of thermal images included in the regression.

The values of the regression analysis in each of the plots distribute around its mean value quite symmetrically, resembling a distribution of errors (standard distribution). The mean value of the different plots changes only by 2% and ranges from 0.638 (if including one thermal image) to 0.626 (regression on 63 thermal images). As the number of thermal images included in the regression analysis increase, the standard deviation of the distribution reduces significantly, resulting in a higher certainty of the results.

By using only one thermal image there is a risk of obtaining values that deviate significantly from the expected value, e.g., the first plot in Figure A4 (one thermal image) includes a measurement with relative high value ($1.3 \text{ W}\cdot\text{m}^{-2}\cdot\text{K}^{-1}$), which contributes to the large spreading of observations in that plot, and also the skewed distribution in Figure 9. That stresses the importance of using several thermal images to obtain accurate results. The effect of this single high measurement value can be observed also in the plots with two and three thermal images; however, after including 10 thermal images its effect diminished and the uncertainty reduced to 11%. Including 27 thermal images was found to reduce the uncertainty to 5%, and 63 thermal images to 3% uncertainty.

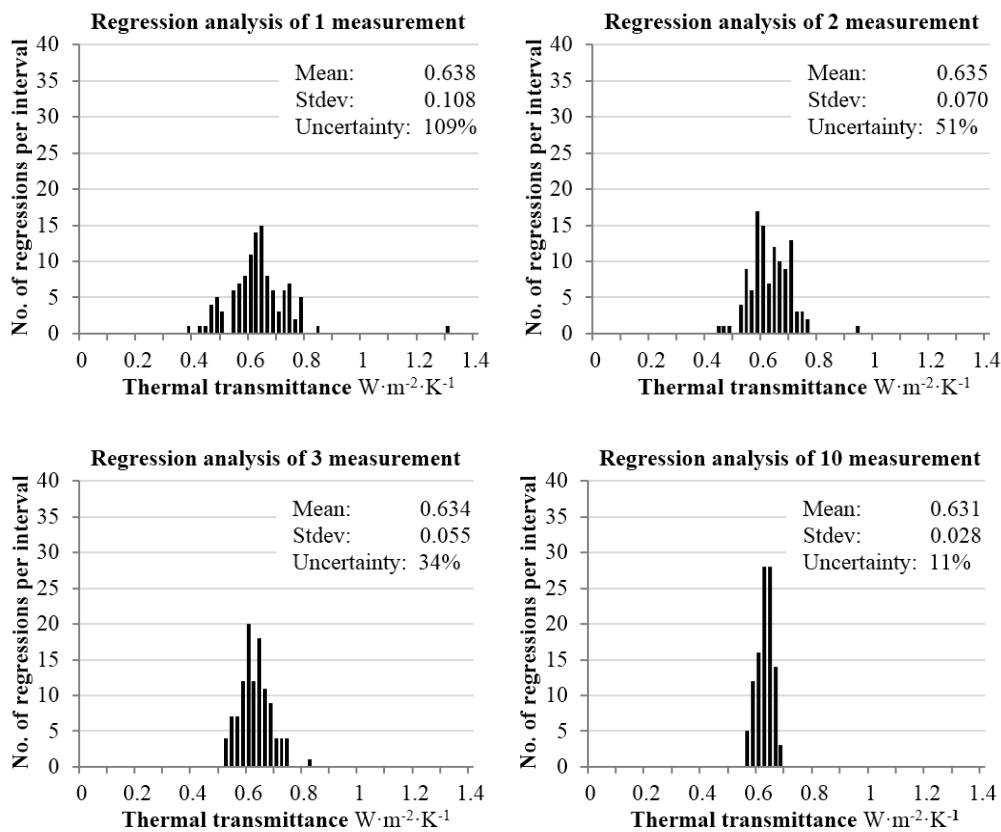


Figure A4. Cont.

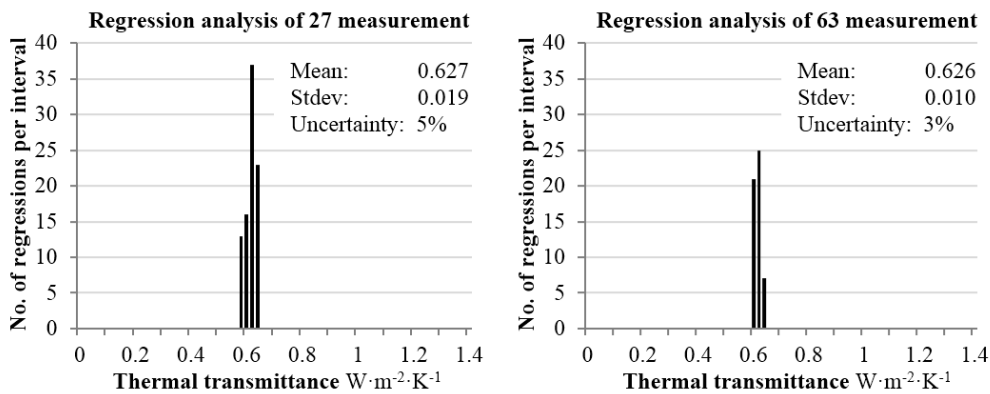


Figure A4. The distribution of the values of the thermal transmittance obtained by regression analysis as described in Section 2.4 in the main article. Each plot represents a different number of thermal images included in the regression analysis.

References

1. Menezes, A.C.; Cripps, A.; Bouchlaghem, D.; Buswell, R. Predicted vs. actual energy performance of non-domestic buildings: Using post-occupancy evaluation data to reduce the performance gap. *Appl. Energy* **2012**, *97*, 355–364. [CrossRef]
2. Danielski, I. Large variations in specific final energy use in Swedish apartment buildings: Causes and solutions. *Energy Build.* **2012**, *49*, 276–285. [CrossRef]

3. Torcellini, P.A.; Pless, S.; Deru, M.; Griffith, B.; Long, N.; Judkoff, R. *Lessons Learned from Case Studies of Six High-Performance Buildings*; Report No.: NREL/TP-550-37542; National Renewable Energy Laboratory: Golden, CO, USA, 2006.
4. Pettersen, T.D. Variation of energy consumption in dwellings due to climate, building and inhabitants. *Energy Build.* **1994**, *21*, 209–218. [[CrossRef](#)]
5. Johnston, D.; Miles-Shenton, D.; Farmer, D. Quantifying the domestic building fabric ‘performance gap’. *Build. Serv. Eng. Res. Technol.* **2015**, *36*, 614–627. [[CrossRef](#)]
6. Pearson, C. *Thermal Imaging of Building Fabric, a BSRIA Guide*; BSRIA 2011 2015. Report No. BG 39/2011. Available online: www.bsria.co.uk (accessed on 1 January 2015).
7. Bauwens, G.; Roels, S. Co-heating test: A state-of-the-art. *Energy Build.* **2014**, *82*, 163–172. [[CrossRef](#)]
8. ISO 9869-1:2014. *Thermal Insulation—Building Elements—In-Situ Measurement of Thermal Resistance and Thermal Transmittance—Part 1: Heat Flow Meter Method*; ISO: Geneva, Switzerland, 2014.
9. Kylili, A.; Fokaides, P.A.; Christou, P.; Kalogirou, S.A. Infrared thermography (IRT) applications for building diagnostics: A review. *Appl. Energy* **2014**, *134*, 531–549. [[CrossRef](#)]
10. IEA. Annex 40 Commissioning of Building HVAC Systems for Improved Energy Performance. In Proceedings of the Fourth International Conference for Enhanced Building Operations, Paris, France, 18–19 October 2004.
11. IEA. Annex 46 Holistic Assessment Tool-Kit on Energy Efficient Retrofit Measures for Government Buildings (EnERGo). Available online: www.iea-ebc.org/Data/publications/EBC_Annex_46_PSR.pdf (accessed on 25 June 2018).
12. Sfarra, S.; Marcucci, E.; Ambrosini, D.; Paoletti, D. Infrared exploration of the architectural heritage: From passive infrared thermography to hybrid infrared thermography (HIRT) approach. *Mater. Constr.* **2016**, *66*, e094. [[CrossRef](#)]
13. Asdrubali, F.; Baldinelli, G.; Bianchi, F. A quantitative methodology to evaluate thermal bridges in buildings. *Appl. Energy* **2012**, *97*, 365–373. [[CrossRef](#)]
14. Grinzato, E.; Ludwig, N.; Cadelano, G.; Bertucci, M.; Gargano, M.; Bison, P. Infrared thermography for moisture detection: A laboratory study and in-situ test. *Mater. Eval.* **2011**, *69*, 97–104.
15. Lerma, J.L.; Cabrelles, M.; Portalés, C. Multitemporal thermal analysis to detect moisture on a building faade. *Constr. Build. Mater.* **2011**, *25*, 2190–2197. [[CrossRef](#)]
16. Fox, M.; Coley, D.; Goodhew, S.; De Wilde, P. Time-lapse thermography for building defect detection. *Energy Build.* **2015**, *92*, 95–106. [[CrossRef](#)]
17. Edis, E.; Flores-Colen, I.; De Brito, J. Time-Dependent Passive Building Thermography for Detecting Delamination of Adhered Ceramic Cladding. *J. Nondestr. Eval.* **2015**, *34*, 24. [[CrossRef](#)]
18. Krankenhagen, R.; Maierhofer, C. Pulse phase thermography for characterising large historical building façades after solar heating and shadow cast—A case study. *Quant. Infrared Thermogr. J.* **2014**, *11*, 10–28. [[CrossRef](#)]
19. Taylor, T.; Counsell, J.; Gill, S. Combining thermography and computer simulation to identify and assess insulation defects in the construction of building façades. *Energy Build.* **2014**, *76*, 130–142. [[CrossRef](#)]
20. Taylor, T.; Counsell, J.; Gill, S. Energy efficiency is more than skin deep: Improving construction quality control in new-build housing using thermography. *Energy Build.* **2013**, *66*, 222–231. [[CrossRef](#)]
21. Perilli, S.; Sfarra, S.; Guerrini, M.; Bisegna, F.; Ambrosini, D. The thermophysical behaviour of cork supports doped with an innovative thermal insulation and protective coating: A numerical analysis based on in situ experimental data. *Energy Build.* **2018**, *159*, 508–528. [[CrossRef](#)]
22. Perilli, S.; Ambrosini, D.; Paoletti, D.; Nardi, I.; de Rubeis, T.; Santulli, C. A proposal of a new material for greenhouses on the basis of numerical, optical, thermal and mechanical approaches. *Constr. Build. Mater.* **2017**, *155*, 332–347.
23. Kordatos, E.Z.; Exarchos, D.A.; Stavrakos, C.; Moropoulou, A.; Matikas, T.E. Infrared thermographic inspection of murals and characterization of degradation in historic monuments. *Constr. Build. Mater.* **2013**, *48*, 1261–1265. [[CrossRef](#)]
24. De Berardinis, P.; Rotilio, M.; Marchionni, C.; Friedman, A. Improving the energy-efficiency of historic masonry buildings. A case study: A minor centre in the Abruzzo region, Italy. *Energy Build.* **2014**, *80*, 415–423. [[CrossRef](#)]
25. Ohlsson, K.E.A.; Olofsson, T. Quantitative infrared thermography imaging of the density of heat flow rate through a building element surface. *Appl. Energy* **2014**, *134*, 499–505. [[CrossRef](#)]

26. Lehmann, B.; Ghazi Wakili, K.; Frank, T.; Vera Collado, B.; Tanner, C. Effects of individual climatic parameters on the infrared thermography of buildings. *Appl. Energy* **2013**, *110*, 29–43. [[CrossRef](#)]
27. Albatici, R.; Tonelli, A.M.; Chiogna, M. A comprehensive experimental approach for the validation of quantitative infrared thermography in the evaluation of building thermal transmittance. *Appl. Energy* **2015**, *141*, 218–228. [[CrossRef](#)]
28. Fokaides, P.A.; Kalogirou, S.A. Application of infrared thermography for the determination of the overall heat transfer coefficient (U-Value) in building envelopes. *Appl. Energy* **2011**, *88*, 4358–4365. [[CrossRef](#)]
29. Sham, J.F.C.; Memon, S.A.; Tommy Lo, Y. Application of continuous surface temperature monitoring technique for investigation of nocturnal sensible heat release characteristics by building fabrics in Hong Kong. *Energy Build.* **2013**, *58*, 1–10. [[CrossRef](#)]
30. Defraeye, T.; Blocken, B.; Carmeliet, J. Convective heat transfer coefficients for exterior building surfaces: Existing correlations and CFD modelling. *Energy Convers. Manag.* **2011**, *52*, 512–522. [[CrossRef](#)]
31. Glulam of Sweden AB (Publ.). Folketshusvägen 6, 840 10 Ljungaverk, Sweden. Available online: <http://www.glulam.se/> (accessed on 1 January 2015).
32. EN ISO 13788:2013. *Hygrothermal Performance of Building Components and Building Elements—Internal Surface Temperature to Avoid Critical Surface Humidity and Interstitial Condensation—Calculation Methods*; SIS, Swedish Standards Institute: Stockholm, Sweden, 2013.
33. Salvaggio, C.; Miller, C.J. Methodologies and protocols for the collection of midwave and longwave infrared emissivity spectra using a portable field spectrometer. In *Aerospace/Defense Sensing, Simulation, and Controls*; International Society for Optics and Photonics: San Diego, CA, USA, 2001; pp. 539–548.
34. ISO 18434-1:2008. *Condition Monitoring and Diagnostics of Machines—Thermography—Part 1: General Procedures*; ISO: Geneva, Switzerland, 2008.
35. Glass, S.V.; Zelinka, S.L. Chapter 4, Moisture relations and physical properties of wood. In *Wood Handbook: Wood as an Engineering Material*; General Technical Report FPL-GTR-190; Department of Agriculture, Forest Service, Forest Products Laboratory: Madison, WI, USA, 2010; pp. 4.1–4.19.



© 2018 by the authors. Licensee MDPI, Basel, Switzerland. This article is an open access article distributed under the terms and conditions of the Creative Commons Attribution (CC BY) license (<http://creativecommons.org/licenses/by/4.0/>).